Effective area of the AXAF high resolution camera (HRC)

D. Patnaude[a], D. Pease[a], H. Donnelly[a], M. Juda[a],
C. Jones[a], S. Murray[a], M. Zombeck [a], R. Kraft[a],
A. Kenter[a], G. Meehan[a], R. Elsner[b], and D. Swartz[c]

[a] Smithsonian Astrophysical Observatory, Cambridge, MA 02138 USA

[b] NASA/Marshall Space Flight Center, Huntsville, AL 35812 USA

[c] Universities Space Research Association, Huntsville, AL 35812 USA

ABSTRACT

The Advanced X-ray Astrophysics Facility High Resolution Camera was calibrated at NASA's X-Ray Calibration Facility during March and April 1997. We have undertaken an analysis of the effective area of the combined High Resolution Mirror Assembly / High Resolution Camera using all data presently available from these tests. In this contribution we discuss our spectral fitting of the beam-normalization detectors, our method of removing higher order contamination lines present in the spectra, and the corrections for beam non-uniformities. Using an approach based upon the mass absorption cross-section of Cesium Iodide, we determine the quantum efficiency in the microchannel plates. We model the secondary electron absorption depth as a function of energy, which we expect to be relatively smooth. This is then combined with the most recent model of the telescope to determine the ensemble effective area for the HRC. The ensemble effective area is a product of the telescope effective area, the transmission of the UV-Ion shield, and the quantum efficiency of the microchannel plates. We focus our attention on the microchannel plate quantum efficiency, using previous results for the UV-Ion shield transmission and telescope effective area. We also address future goals and concerns.

Keywords: Detectors, X-rays, Calibration

1. INTRODUCTION

The Advanced X-ray Astrophysics Facility (AXAF) consists of a high resolution ($\lesssim 1/2$ arcsecond) X-ray telescope and a suite of imaging and spectroscopy instruments. The High Resolution Camera (HRC) consists of two instruments positioned in the focal plane of the High Resolution Mirror Assembly (HRMA): the HRC-I, used for imaging, and the HRC-S, which is used, in conjunction with the Low Energy Transmission Grating, for spectroscopy. The HRC, in conjunction with the HRMA, was calibrated to determine the convolved effective area of the observatory, which is the crucial element an observer must have to convert detected count rates into a source flux. Embedded in the convolved effective area is the quantum efficiency of the detector and the mirror's effective area.

Between March 19th and April 10th, 1997, the HRC underwent an extensive calibration at NASA's X-ray Calibration Facility (XRCF) at the Marshall Space Flight Center in Huntsville, Alabama. The XRCF includes a source building connected to an 18m by 6m instrument chamber by a 518m evacuated X-ray pipe. The source building, known as the X-ray Source System (XSS), consists of four X-ray sources: an Electron-Impact Point Source (EIPS), a Double-Crystal Monochromator (DCM), a High-Resolution Erect Field Spectrometer (HIREFS), and a Penning Ionization Gas-discharge Source (PIGS). Weisskopf *et al.* (1997) give a complete discussion of the XSS as well as an overview of the entire AXAF calibration effort.

The calibration of the HRC effective area involved simultaneously exposing the HRC, in the focal plane of the HRMA, and a set of Beam Normalization Detectors (BND) to X-rays. The BNDs consisted of a set of four Flow Proportional Counters (FPC) positioned around the perimeter of the HRMA entrance aperture, denoted as BND-HN, BND-HS, BND-HT, and BND-HB for the north, south, top and bottom quadrants respectively. A fifth FPC

Other author information: (Send correspondence to D.Patnaude)
D.P.: E mail: patnaude@head-cfa.harvard.edu; Telephone: 617-495-7264; Fax: 617-495-7356

(FPC–500), used for beam mapping, as well as a Solid State Detector (SSD–500), were positioned 38m from the source.

The HRC-I is intended for wide field high resolution imaging, with a geometrical area of 93 mm $\times$ 93 mm. In combination with the HRMA's 10m focal length, this provides a field of view $\sim 31' \times 31'$. The detector consists of a pair of microchannel plates (MCP) in a chevron configuration coated with a CsI photocathode, and a crossed grid charge detector. The CsI photocathode enhances the photoelectric response of the MCPs, which provide an electron avalanche of $\sim 2 \times 10^7$ electrons per incident photon. An aluminized polyimide UV-Ion shield (UVIS) is positioned in front of the MCP and is designed to block low energy electrons and ions, as well as extreme ultraviolet photons. See Kenter *et al.*(1997) for a preliminary report on the HRC-I.

The HRC-S is designed to be the readout detector for the Low Energy Transmission Grating (LETG). However, during the HRC effective area measurements, the HRC-S was used in imaging mode (*i.e.*without the grating), to facilitate the independent calibration of the grating and also in the event that the HRC-S is required as a backup imager. The HRC-S consists of three segments (100 mm $\times$ 20 mm) of stacked microchannel plate pairs placed end to end, coated with a CsI photocathode, in front of a single crossed grid charge detector. When combined with the LETG, the HRC-S bandpass using all three plates is $3 - 160$Å, with a spectral resolution of < 0.1Å over $40 - 160$Å. However, for the measurements described here only the central MCP was used. A preliminary report on the performance of the HRC-S was made by Kraft *et al.*(1997).

The HRC on-axis effective area measurements were performed at 63 energies ranging from ~ 110 eV up to 9 keV. Not all energies could be used to derive quantum efficiencies because of incomplete data and archiving problems. In total 56 and 60 energies for the HRC-I and HRC-S respectively were available for our analysis. All of these measurements were taken out of focus to protect the detector from permanent gain degredation. The focal plane rates were determined by placing a 750 pixel radius (~ 4.82 mm) aperture around the defocused image. An annulus from 800 pixels (~ 5.14 mm) to 900 pixels (~ 5.78 mm) was used for background subtraction.

The HRC's intrinsic (non-dispersive) spectral resolution is limited ($E/\Delta E \sim 1$), which means that even two discrete spectral lines appear as a single broad feature in the output PHA. Unfortunately, while the monochromators were designed to generate a single spectral line, they often produced multiple orders, as well as contamination from the Tungsten source anode. Since the majority of the effective area measurements were performed with the HIREFS or DCM, this required that the fluxes from "contaminating" lines first be measured in the BND spectra. Then their contribution to the HRC's output count rate must be modeled and removed before we could properly characterize the quantum efficiency at the energy of interest. Our procedure for handling this is discussed in detail in § 3.

By comparing the X-ray flux density in front of the HRMA with the count rate detected in the focal plane, one should be able to determine the HRMA/HRC effective area. However, due to various problems such as low flux and beam non-uniformity, we were required to use a more complicated approach which involved applying beam uniformity corrections and weighting the flux based upon the mirror effective area. We discuss this in § 2.2.

Finally, in § 4.and § 5.we discuss our results and issues which are still pending in our analysis of the instrument.

2. BEAM NORMALIZATION DETECTOR DATA ANALYSIS

2.1. PHA Analysis

The ultimate goal behind the spectral fitting procedure was to model the incident source flux. In general, this consisted of the flux in a set of spectal lines, plus a set of parameters describing the flux per keV in the continuum. For the case of the HRC effective area measurements this problem is greatly simplified because the vast majority of the measurements were performed with the monochromators (which, by definition, have no continuum component). Those few measurements made with the EIPS contained a filter which was designed to block out the continuum. The problem then reduced to modelling the flux $F_k(E_i)$ in the i^{th} line observed by the k^{th} BND.

We have chosen to use the Jahoda-McCammon-Kramer model (JMKmod) adapted by the AXAF Mission Support Team (MST) for fitting within the XSPEC X-ray spectral fitting package. JMKmod convolves a model of an X-ray source spectrum with a model of the reponse of an FPC. The model contains a number of parameters which can be divided into three distinct groups: instrumental parameters which did not change from detector to detector, variable detector parameters (e.g. Fano factor and various model normalizations*), and variable source parameters (e.g. line energy, filters, and high voltage). The advantage of using JMKmod versus simpler functions (Gaussian, Prescott, etc.) is that JMKmod gives a physical representation of the source/detector system, which can be adjusted as more is learned about the FPC. The full functionality of the model is discussed in Tsiang *et al.*(1997) and Tsiang (1997).

Several complications arose in the spectral fitting because the XSS was run in low-flux mode to avoid gain degredation in the HRC. In particular, the BND background made a non-negligible contribution to the count rate. To correct for this, we fit background measurements taken independently with a power-law – for a tail in the lower channels– combined with a broad Gaussian ($\sigma \approx 400$ channels) for the entire detector. This was then combined, as a constant component, with the rest of the JMKmod in XSPEC. This approach avoided the unphysical situation of channels with negative counts, which often resulted from a manual background subtraction. A typical BND spectrum is shown in Figure 1. In this figure, JMKmod fits the two spectral components, but above channel 360 the data is fit better by the background model. The low channel noise is not very evident in this example due to a shelf from channels 40–100. This type of shelf, which was common in the data, was caused by incomplete charge transfer in the FPC gas (Edgar, *et al.*, 1997).

Another result of the intrinsically low signal-to-noise was the underestimation of model normalizations. Cash (1979) has shown that a standard χ^2 treatment of data with few counts per bin leads to an underestimation of the fit in the wings (Bevington 1992). A better method involves using a maximum likelihood estimator, also known as a C-statistic. A comparison of the results of fitting identical datasets with the two methods indicates that χ^2 minimization can underestimate our fit global and line normalizations by as much as $\sim 20\%$. As a result, we chose to use the C-statistic for our spectral fitting.

We begin the analysis of a BND PHA by determining the count rate in the i^{th} line, $R_k(E_i)$, in each BND. This is determined from the fits by the global normalization for the k^{th} BND (N_k^{global}), and the fractional normalization for the i^{th} line ($N_k(E_i)$):

$$R_k(E_i) = N_k^{global} \times N_k(E_i) \qquad cts\ s^{-1}. \tag{1}$$

This rate is then divided by the open area of the FPC, A_k, and the detector quantum efficiency $\eta_k^{BND}(E_i)$, to determine the modeled flux at the k^{th} BND ($F_k(E_i)$):

$$F_k(E_i) = \frac{R_k(E_i)}{A_k \times \eta_k^{BND}(E_i)} \qquad photons\ s^{-1}\ cm^{-2}. \tag{2}$$

The errors are statistical and are added in quadrature.

In principle we can then determine the telescope/detector effective area ($A'_{total}(E_i)$) given by:

$$A'_{total}(E_i) = \frac{R^{FP}(E_i)}{< F(E_i) >} \qquad cm^2, \tag{3}$$

where $R^{FP}(E_i)$ is the count rate in the focal plane detector, and we have assumed that $< F(E_i) >$ is the flux averaged over the four BNDs. Because there were large spatial variations in intensity across the front of the HRMA, this was not representative of the average flux. To correct for this effect we have used a beam uniformity analysis provided by the AXAF Project Science group to appropriately weight the fluxes measured by each BND.

*The normalizations include the global normalization (N_{global}) and the line normalization ($N(E_i)$). These two normalizations are combined in the model such that the total count rate in the line is determined by the product of the two.

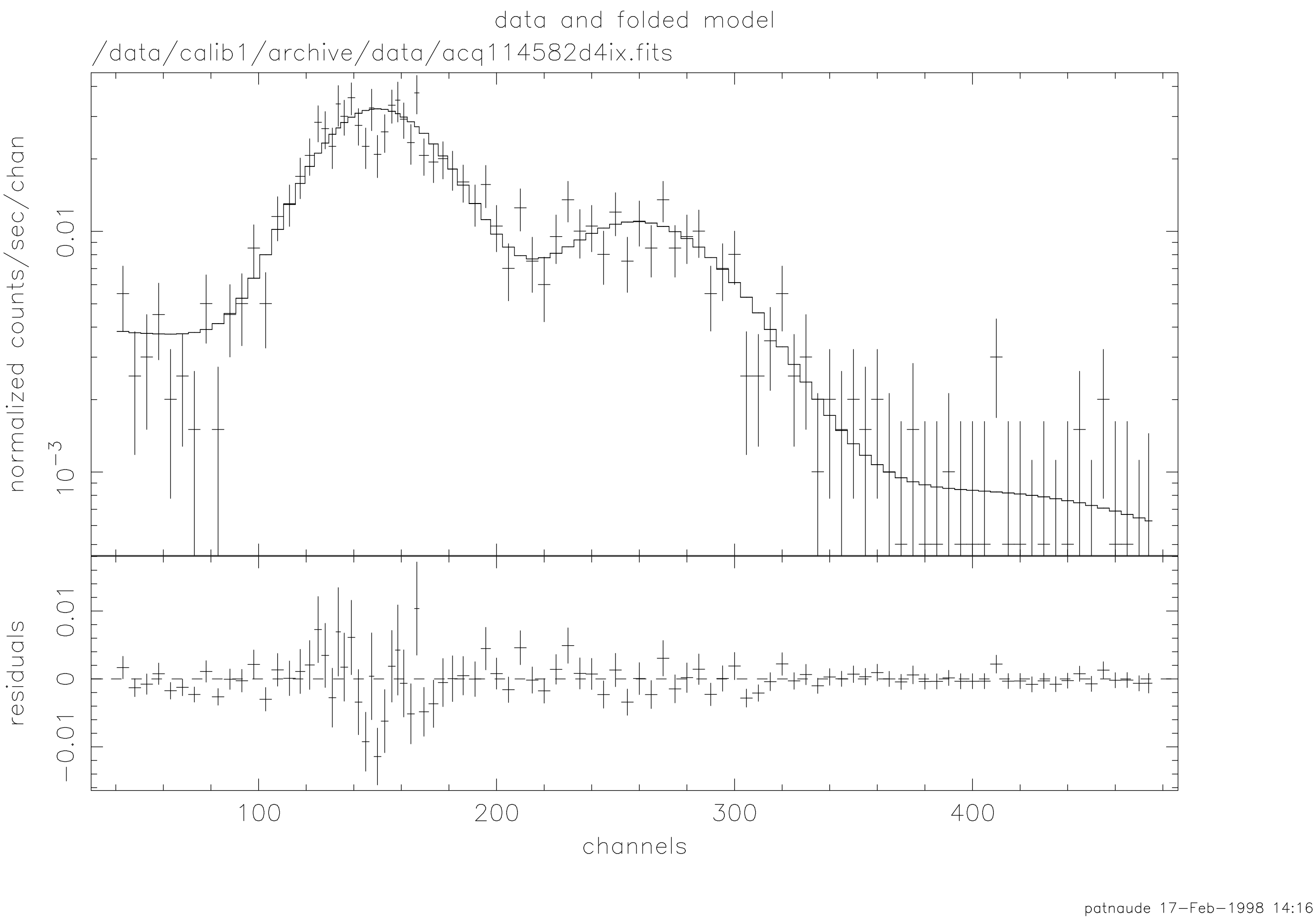

Figure 1. Example BND PHA from a HIREFS measurement showing a second order contribution. The primary energy is 900 eV, but there is a significant contribution from 1800 eV.

2.2. Beam Uniformity Analysis

For some of the source settings, a map of the beam was generated to determine the spatial intensity of the source. For each map, the FPC–500 measured the average flux at each quadrant-shell position of the HRMA. This data was fit with a polynomial and Gaussian to produce a surface describing the beam.

We first determined the modeled flux per unit source current incident on the focal plane. This is the product of the beam uniformity modeled average flux density ($F^{PS}_{q,s}(E_i)$) at each of the 16 quadrant–shell (q, s) positions and the appropriate mirror effective area ($A'_{q,s}(E_i)$):

$$\tilde{F}_{q,s}(E_i) = A'_{q,s}(E_i) \times F^{PS}_{q,s}(E_i) \qquad photons\ s^{-1}\ mA^{-1}. \tag{4}$$

This weighted the flux with the mirror effective area, allowing a direct sum over the quadrants and shells, giving a total photon rate per mA ($\mathcal{F}(E_i)$) at each energy incident upon the focal plane. The errors are independent, and were added in quadrature.

The ratio, $\lambda_q(E_i)$, of our modeled flux density in a BND ($F_k(E_i)$) from Equation 2 to the flux density per mA in the same BND modeled from the beam uniformity maps ($F^{PS}_k(E_i)$) gives the scale factor (i.e. current) required to get the photon rate incident on the focal plane detector:

$$\lambda_k(E_i) = \frac{F_k(E_i)}{F^{PS}_k(E_i)} \qquad mA. \tag{5}$$

Each scaling factor was applied to the modeled focal plane photon rate per milliamp, $\mathcal{F}(E_i)$, to generate a photon rate $(f_k(E_i))$ incident on the focal plane as projected by each BND:

$$f_k(E_i) = \mathcal{F}(E_i) \times \lambda_k(E_i) \ , \tag{6}$$

The four values $(f_k(E_i))$ were then averaged to determine the photon rate incident upon the focal plane for the i^{th} line $(\overline{\mathcal{F}}(E_i))$. The average was weighted with the errors $\sigma_{f_k(E_i)}$ in order to account for a systematic bias in the scaling factor in the north detector between 0.6 and 1.5 keV, which was purely an artifact of the polynomial fits:

$$\overline{\mathcal{F}}(E_i) = \frac{\sum_k f_k(E_i)/\sigma^2_{f_k(E_i)}}{\sum_k (1/\sigma^2_{f_k(E_i)})} \qquad photons\ s^{-1}, \tag{7}$$

It is worth noting that if the beam were perfectly uniform, the scale factor, $\lambda_k(E_i)$, would be equal to the source current used for the beam uniformity map, and the projected rate would be equivalent to the average BND flux multiplied by the mirror effective area.

In the case where no beam uniformity data exists (as well as data taken with the EIPS), a less complex method was used which involved averaging the modeled flux $(F_k(E_i))$ in each BND and using the total HRMA effective area to get an incident photon rate.

Once the incident rate was determined at each energy, we determined the quantum efficiency of the HRC by comparing the incident rate to the detected count rate. We then generated a continuous curve for the quantum efficiency. This was then used in conjunction with the HRMA effective area to generate an ensemble effective area for the HRMA/HRC system.

3. MCP QUANTUM EFFICIENCY ANALYSIS

As noted above, a lack of spectral resolution in both the HRC-I and HRC-S made it difficult to analyze the multi-component spectra sometimes produced by the monochromators. For instance, the HIREFS produces multiple orders up to the M edge of Gold at 2 keV (*i.e.* A HIREFS setting of 600 eV would generate lines at 600 eV, 1.2 keV, and 1.8 keV). There is also contamination from two groups of Tungsten M lines at ~ 1.38 and ~ 1.77 keV, which appear in all the spectra though with varying power. A further complication was that often the count rate in contamination lines was significantly higher than the rate from the line of interest. We have identified three distinct and progressively more complex spectra.

The first set consists of measurements taken right at the Tungsten contamination lines. At 1.38 keV, the flux is almost solely due to Tungsten line located there. The 1.77 keV line is present but extremely weak– $\sim 1\%$. At 1.77 keV the sense of the ratio is reversed, although the 1.38 is moderately strong, contributing $\sim 20\%$ of the flux. Because these lines were present in all the other spectra, we began by first analyzing the data at 1.38 keV and then using this to bootstrap our analysis for the 1.77 keV line.

From here we proceeded to the second set of spectra which had energies above 1 keV. Because this energy range was not susceptible to higher order contamination the spectra consisted of the line of interest and the Tungsten contamination lines.

Finally, we were prepared to work on the data from energies below 1 keV, where we found the Tungsten contamination lines as well as higher order lines. This process obviously had the potential of propagating substantial errors, so it was important to determine the photon flux in each line as accurately as possible. Our final results indicate that we have had mixed success in determining the effective area below 1 keV, especially when third order lines– thus four contaminating lines, i.e. two higher order lines plus the two Tungsten lines– are present.

With multiple lines present in the source spectra, we first determined the HRC count rate $(R'(E_{i\neq1}))$ in each line other than the principle line ,E_1, at which the source was tuned. In general:

$$R'(E_{i\neq1}) = \overline{\mathcal{F}}(E_{i\neq1}) \times \eta'(E_{i\neq1}) \qquad counts\ s^{-1}, \tag{8}$$

where $\overline{\mathcal{F}}(E_{i\neq 1})$ is the flux incident upon the detector (as calculated from Equation 7 or Equation 2) and the HRC quantum efficiencies $\eta'(E_{i\neq 1})$, are previously determined via our bootstrapping process. Then,

$$R''(E_1) = R_{TOT} - \sum_{j\neq 1} R'(E_j) \tag{9}$$

and,

$$\eta''(E_1) = \frac{R''(E_1)}{\overline{\mathcal{F}}(E_1)} \quad . \tag{10}$$

Once the quantum efficiency ($\eta''(E_1)$) of the detector (UVIS and MCP) was determined at each discrete energy, we divided out the transmission of the UVIS (η_{UVIS}) to arrive at the quantum efficiency of the MCP (η_{MCP}). This is a function of how easily the electrons generated by the absorption of an X-ray can escape the photocathode. The electrons fall into two categories: primary electrons, consisting of those ejected by the photoelectric effect or Auger transitions, and secondary electrons produced by the interaction of the primary electrons with the photocathode. The primary electrons have an energy proportional to the incident photon, while the energy of the secondary electron is very nearly 1 eV, independent of incident photon energy (Henke, *et al.*1981). Nominally, the combined yield of primary and secondary electrons should determine the quantum efficiency. Due to the complex physics of the photocathode deposited on the front of the MCP (Murray, 1988) the data is unfortunately neither smooth nor easily described by a single function.

Instead we opted to fit the absorption range of the secondary electrons produced by each photon interaction (Juda 1997). Nominally, this is a smooth and continuous function as all the edge structure has been removed. In practice however, although the smoothness and continuity of the data has improved significantly, it still requires several components.

We have defined the absorption range of the secondary electrons as:

$$\mathcal{L}(E) = \frac{-\ln(1 - \frac{\eta_{MCP}(E)}{f_{pore}})}{\mu\rho_{CsI}(E) \cdot \rho_{CsI}}, \tag{11}$$

where $\eta_{MCP}(E)$ is the HRC quantum efficiency, f_{pore} is the packing fraction of the MCP, ρ_{CsI} is the bulk density of Cesium Iodide, and $\mu\rho_{CsI}(E)$ is the mass absorption cross section at E.

We found that there are several regimes requiring separate fits, possibly indicating edge structure for which we have not accounted or accounted for incompletely. We have empirically fit the range versus the energy on a log–log scale with quadratic functions ($\Lambda(E)$) for each region.

By inverting equation 11,

$$\eta_{model}(E) = (1 - \exp^{-y(E)}) \cdot f_{pore} \ , \tag{12}$$

where

$$y(E) = \Lambda(E) \cdot \rho_{CsI} \cdot \mu\rho_{CsI}(E) \ , \tag{13}$$

and using our newly generated range values ($\Lambda(E)$), we generated a curve modeling the MCP quantum efficiency. This was then recombined with the UVIS transmission and HRMA effective area to give us the full HRC/HRMA effective area.

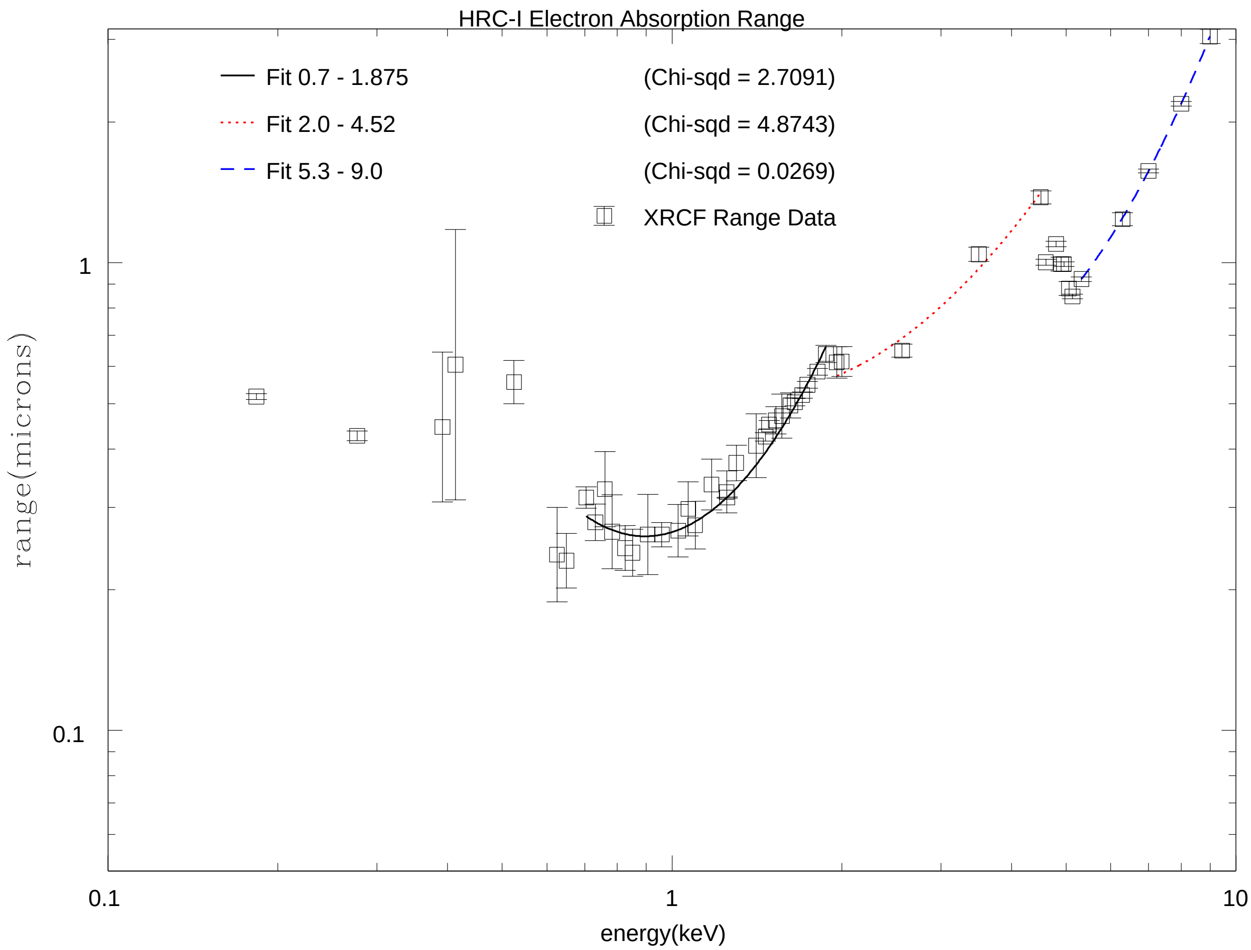

Figure 2. Effective range of secondary electrons in the HRC-I MCP

4. RESULTS

4.1. HRC-I

From Figure 2 we have identified three regions: from 5.32 keV to 9 keV, from 2 keV to 4.51 keV and below 1.875 keV. In all three regions a quadratic fit provided significantly better fit than a linear solution. Between 4.51 and 5.32 keV there is an obvious discontinuity in the range data due to a series of Cesium and Iodine absorption edges (Fraser *et al.*, 1995). We have used a simple linear interpolation between the data points in conjunction with synchrotron data – to locate the edges– to produce a fit in this region.

We are uncertain about the source of the discontinuity at 2 keV. It is possibly due to residual errors in the mirror effective area in that region, due to an edge at 2 keV. Small deviations in the mirror effective area would have a substantial impact on the calculated range of the detector. For the time being we have simply separated the data above and below this boundary into separate fits.

As we proceed to lower energies from 2 keV, we find that the quality of the results declines. This is most likely due to a progressive increase in the uncertainty due to the removal of multiple orders discussed above. This is further complicated by the sensitivity of the calculated quantum efficiency to small changes in incident flux and count rate. Between 700 eV and 1.82 keV the data appears reasonably well behaved and we have selected this region for our range fitting procedure. Furthermore, an extrapolation of this fit to lower energies produces unphysical results. We note that the cutoff point that we have selected based on the data quality coincides with the energies where contamination by third order lines becomes possible.

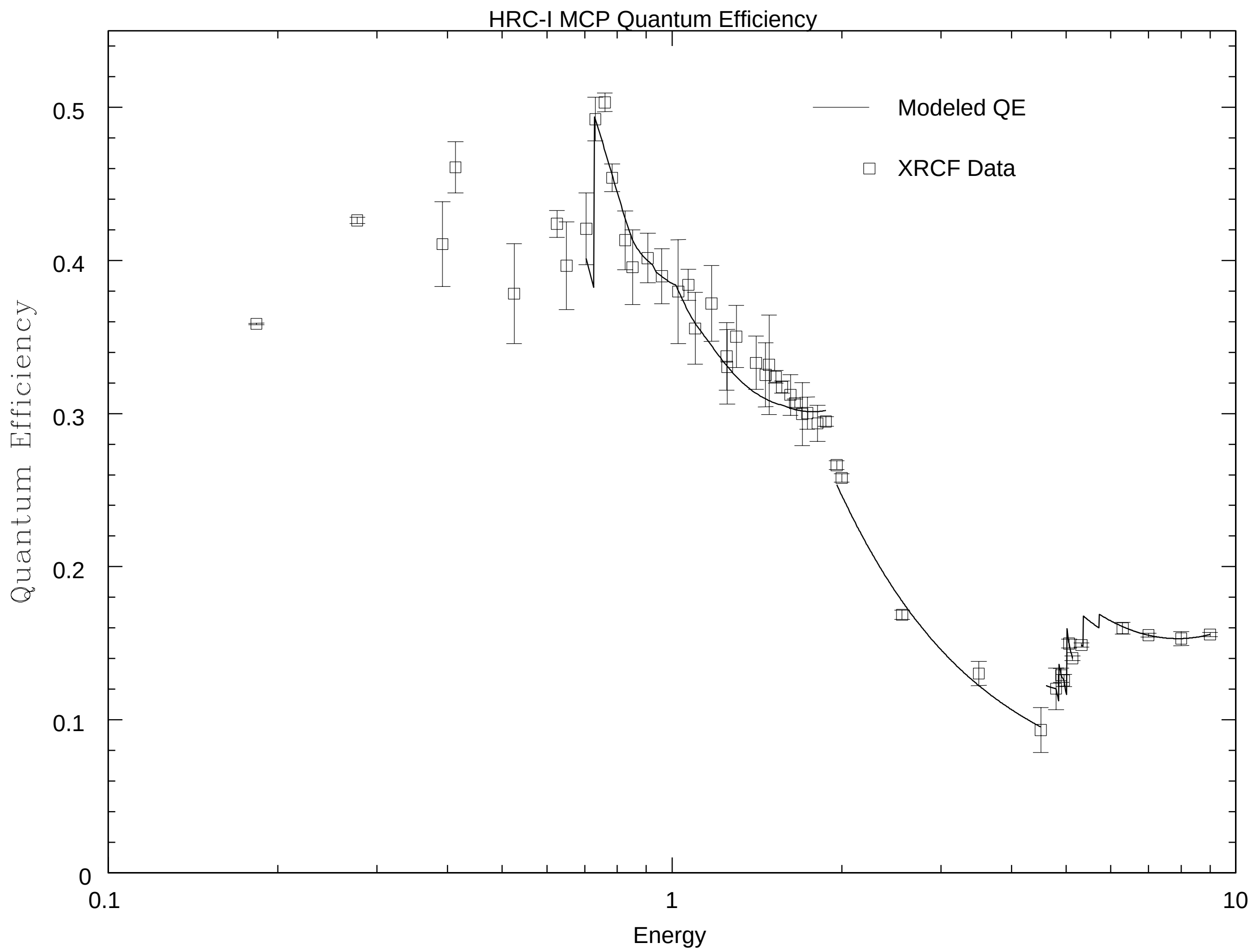

Figure 3. Modeled MCP quantum efficiency between 700 eV and 9 keV.

The curve in Figure 2 was then used with Equation 12 to generate the model for the MCP quantum efficiency (Figure 3). Combining our results with the UVIS transmission (Meehan, *et al.*, 1997), as well as the most recent HRMA effective area (Jerius, 1998) yielded our model for the HRC-I/HRMA effective area (Figure 4).

The original instrument team model between 0.7 and 2 keV was a conservative estimate (Murray, 1998) lending confidence to our higher result. We have also included a Ring Focus measurement made with the EIPS Mg anode at 1.254 keV. The EIPS source spectrum did not have any order contamination and had a very weak continuum component, resulting in a very robust measurement of the efficiency at this energy. Happily the calculated efficiency is in good agreement with the HIREFS data taken at 1.25 keV. Above 2.0 keV, we find excellent agreement with subassembly calibration data taken by the HRC Instrument team (Kenter, 1997). As noted above, below 700 eV our data is in poor agreement with all available models. We note however, that the C-K_α line does agree with the instrument team predictions. Below 700 eV we have directly incorporated the instrument team results into our model.

4.2. HRC-S

Our analysis of the HRC-S's quantum efficiency proceeded similarly to that described for the HRC-I above. Producing a range plot with, as one would expect, extremely similar features. The data below 700 eV still appears to be

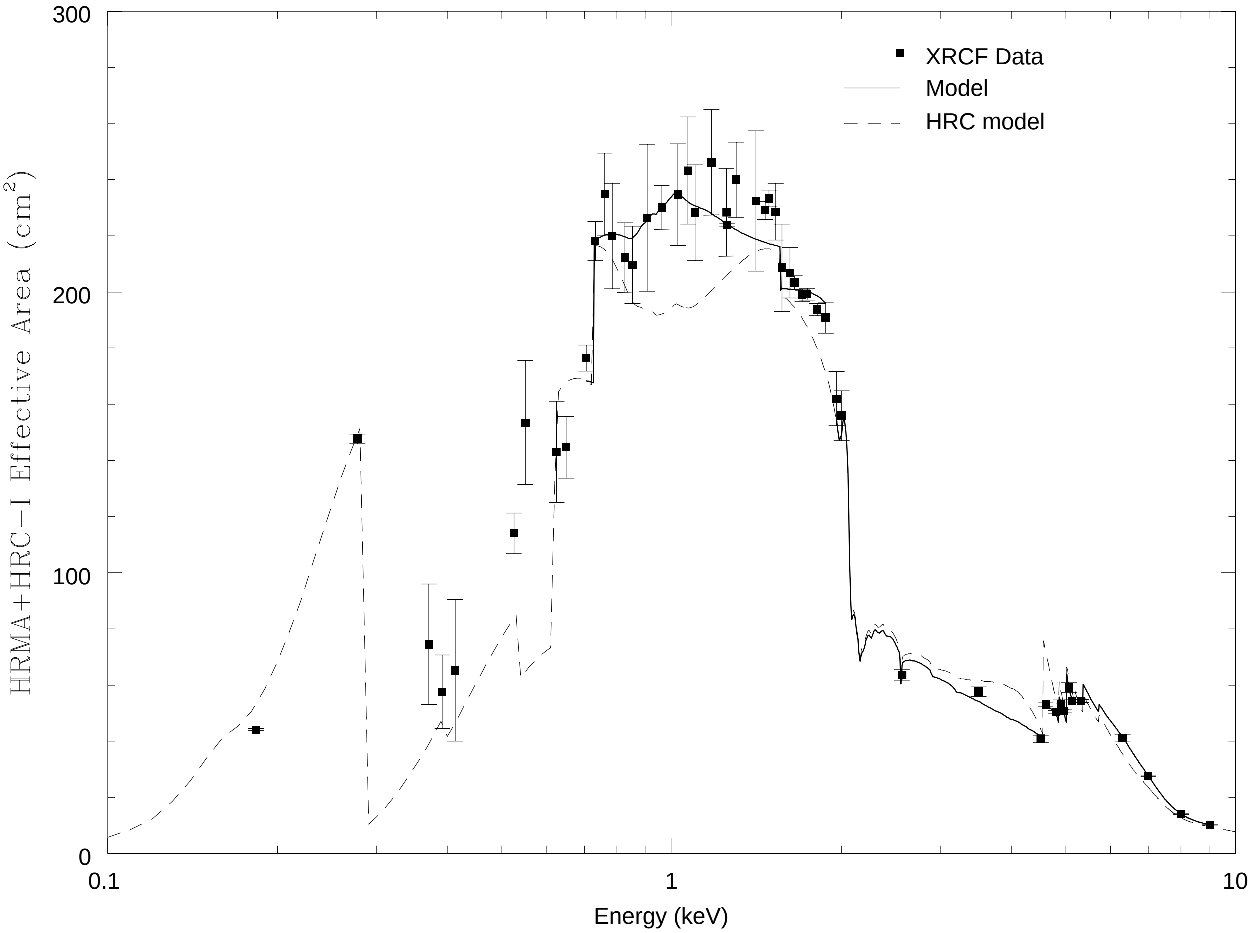

Figure 4. Modeled effective area (solid curve) for the HRC-I as compared to the HRC Instrument Team modeled effective area (dashed curve). We have adopted the instrument team model below 700 eV.

unreliable and was again excluded from our fits. Furthermore, based on our experiences with the HRC-I and the expected similarity of the two detectors, we have divided the data into the same three energy regimes.

Figure 5 shows the results of our quadratic fits to the three energy regimes in the data. Figure 6 gives the HRC-S quantum efficiency and Figure 7 the convolved HRMA/HRC-S effective area . As with the HRC-I, we have adopted the instrument team model below 700 eV.

After completion of the testing at the XRCF, the HRC-S was modified slightly to improve the gain and quantum efficiency. Following these modifications, a series of lab measurements were performed by the HRC IPI team to provide data to bootstrap the XRCF results to the flight configuration. Those corrections towards a flight model are still pending, but should be available to the general user public later this summer.

5. FUTURE DIRECTIONS

There are several outstanding issues which we must address in order to complete a more thorough calibration of the HRC. First, we need to determine the meaningfulness for our JMKmod fits. While our fits model the data extremely well, it is not clear if the detector parameters are physically reasonable.

Second, absolute quantum efficiency curves with errors are needed for each BND. Currently, we rely on fits provided by MST where we have assumed an average uncertainty of 5% in the fits. These fits are the result of

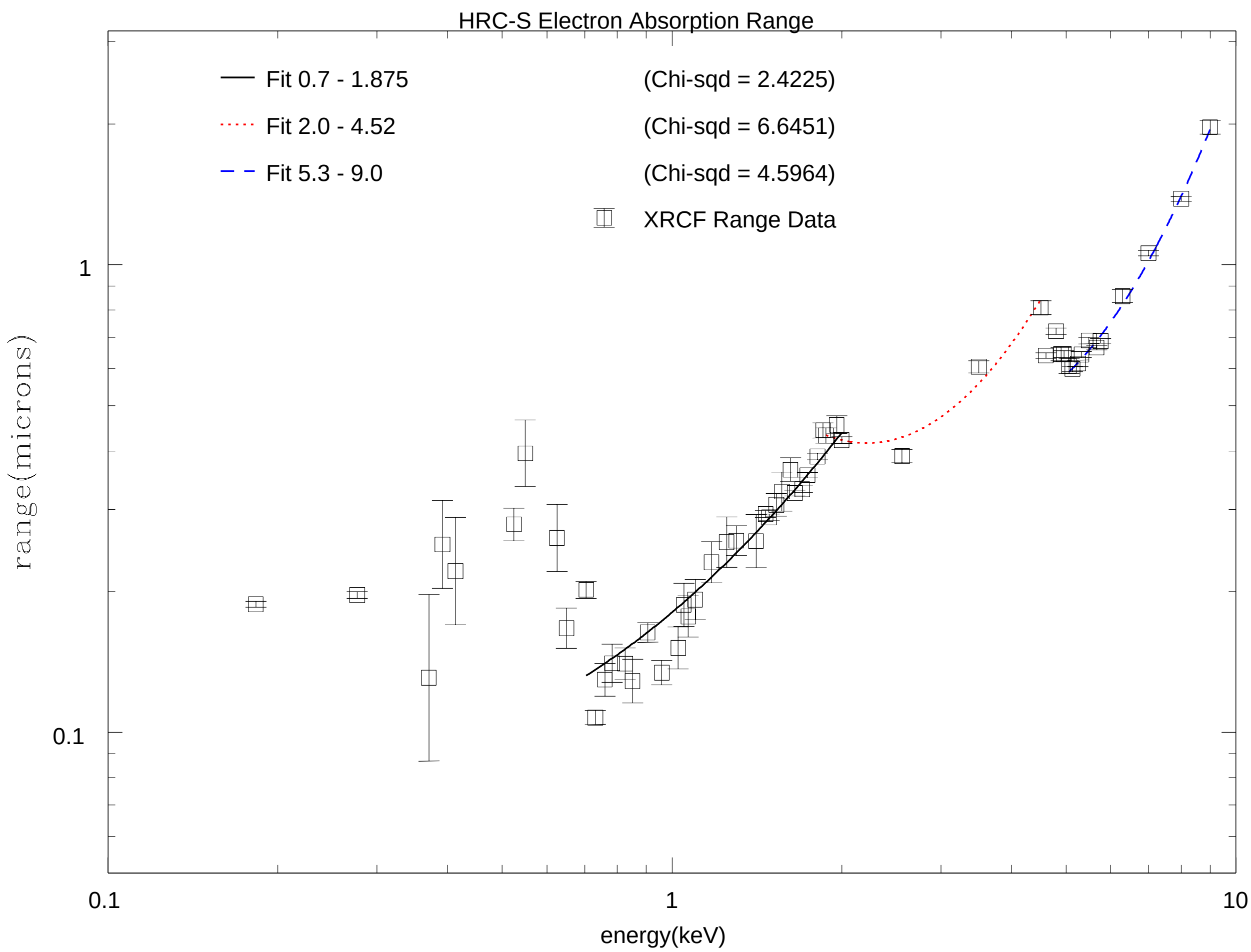

Figure 5. Range of secondary electrons in the HRC-S MCP.

measurements taken with the AXAF CCD Imaging Spectrometer (ACIS) "I3" chip (Wargelin, *et al.*(1997)). We anticipate that the forthcoming absolute efficiency curves based on synchrotron measurements will help increase the certainty of our models.

Third there were several synchronization problems which have hindered our efforts at correlating the various datasets taken during a measurement. We will rely on the AXAF Science Center Data Systems (ASCDS) to correct these clock problems to ensure that all data is available for analysis.

Finally, models of the source beams spatial distribution are needed at the energies other than those for which beam maps were performed. As more realistic models of the monochromator beams become available, they will replace the method of straight averaging we currently rely upon.

Our ultimate goal is to produce a model of the performance of the HRC on orbit. This will require the merging of all of the work presented here with the subassembly results generated after the adjustment of the HRC following the XRCF (Murray *et al.*, 1997). The final achievement will be one of the best characterized X-ray instruments available.

ACKNOWLEDGEMENTS

We wish to thank Dick Edgar and the entire Mission Support Team for many useful conversations regarding the spectral fitting of FPC data. We would also like to thank the ASCDS for a timely reprocessing of the photon event

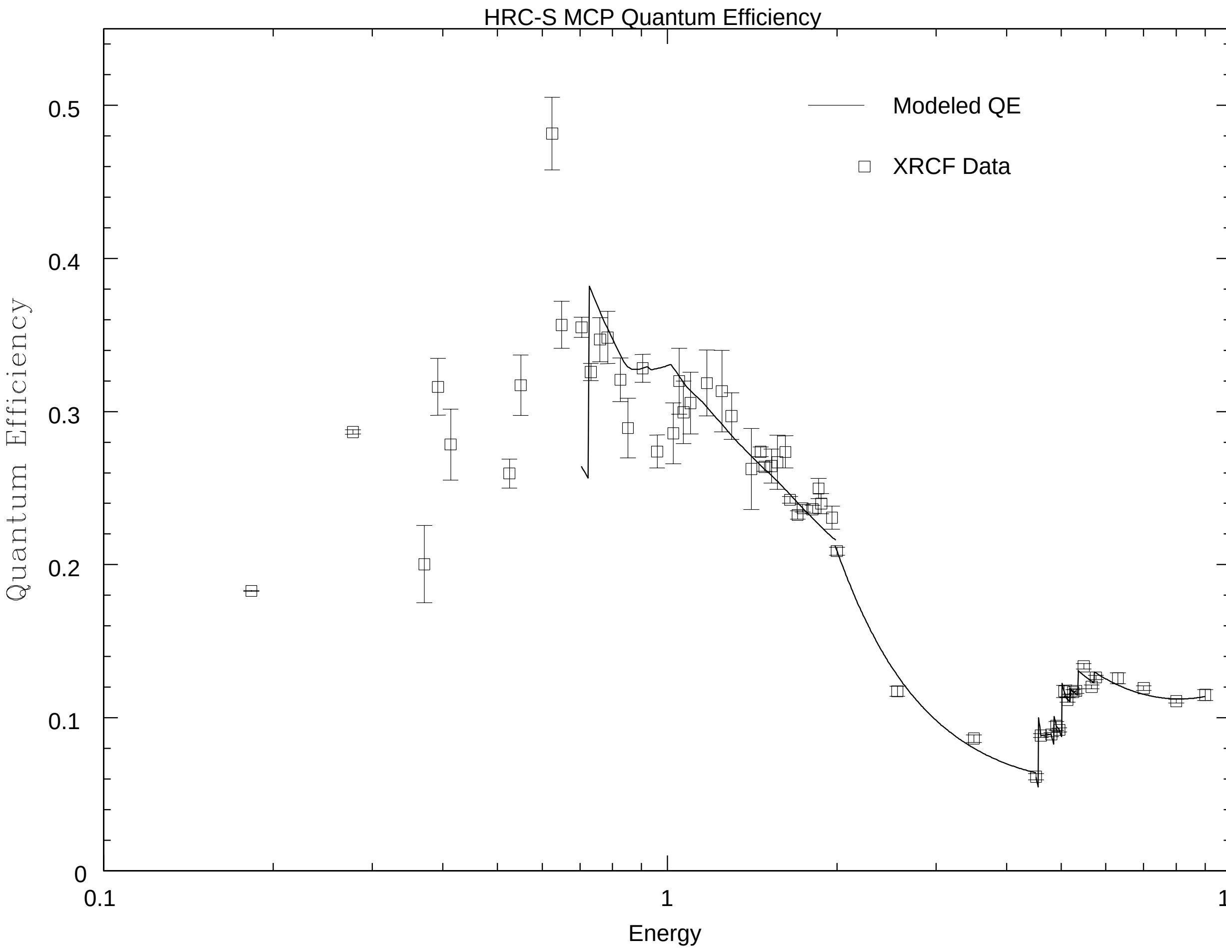

Figure 6. Modeled MCP quantum efficiency for the HRC-S central MCP.

lists. Finally, we would like to thank the Project Science team for their help in understanding the beam uniformity issues, and their responsiveness to questions we have posed regarding their separate analysis.

REFERENCES

.

Arnaud, K.A., 1996, *Astronomical Data Analysis Software and Systems V*, eds. Jacoby G. and Barnes J., p17, ASP Conf. Series volume 101.

Bevington, P. R., & Robinson, D. K. *Data Reduction and Error Analysis for the Physical Sciences* (New York: McGraw Hill), 1992.

Cash, W. "Parameter estimation in astronomy through application of the likelihood ratio", ApJ **228**, pp. 939-947, 1979.

Edgar, R. "Spectral Fitting in AXAF Calibration Detectors," in *Grazing Incidence and Multilayer X-ray Optical Systems*, R.B. Hoover and A.B. Walker, eds., *Proc SPIE* **3113**, pp. 124-131, 1997.

Fraser, G.W., Pearson, J.F., Lees, J.E., Pearce, S.E., Brunton, A.N., Flanagan, K.A., Kenter, A.T., Barbera, M. "Synchrotron calibration of alkali halide–coated microchannel plate detector in the 50-350 and 2000-6000 eV bands", *Proc SPIE* **2518**, pp. 322-335, 1995.

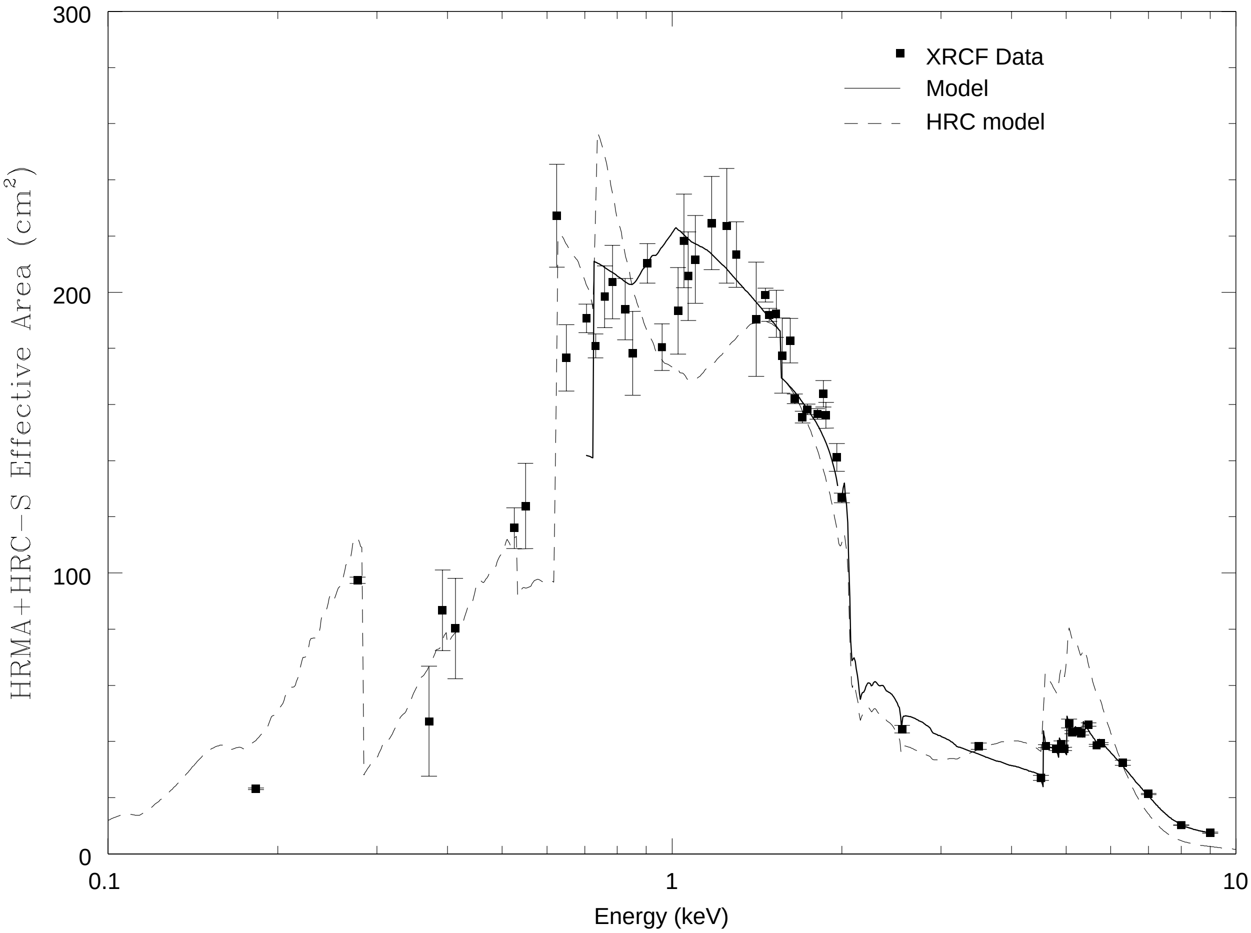

Figure 7. Modeled effective area (solid curve) compared to the HRC Instrument Team modeled effective area (dashed curve)for the HRC-S. As with the HRC-I, below 700 eV where our fitting is inadequate we have incorporated the model developed by the instrument team.

Henke, B.L., Knauer, J.P., Premaratne, K. "The characterization of x-ray photocathides in the 0.1–10 keV photon energy region", J. Appl. Phys **52(3)**, pp. 1509-1520, 1981.

Jahoda, K., and McCammon, D. "Proportional Counters as Low Energy Photon Detectors", Nuclear Instr. and Methods **A272**, pp. 800-850, 1988.

Jerius, D. *Private Communication* 1998.

Juda, M. "A simple model for the QE of CsI coated MCPs", ASC Memorandum, 1997.

Kenter, A.T., Chappell, J.H., Kobayashi, K., Kraft, R.P., Meehan, G.R., Murray, S.S., Zombeck, M.V., Fraser, G.W., Pearson, J.F., Lees, J.E., Brunton, A.N., Pearce, S.E., Barbera, M., Collura, A., Serio, S. "Performance and Calibration of the AXAF High Resolution Camera I: the Imaging Detector", SPIE **3114**, pp. 26-52, 1997.

Kraft, R.P., Chappell, J.H., Kenter, A.T., Kobayashi, K., Meehan, G.R., Murray, S.S., Zombeck, M.V., Fraser, G.W., Pearson, J.F., Lees, J.E., Brunton, A.N., Pearce, S.E., Barbera, M., Collura, A., Serio, S. "Performance and Calibration of the AXAF High Resolution Camera II: the Spectroscopic Detector", SPIE **3114**, pp. 53-73, 1997.

Meehan, G.R., Murray, S.S., Zombeck, M.V., Kraft, R.P., Kobayashi, K., Chappell, J.H., Kenter, A.T., Barbera, M., Collura, A., Serio, S., "Calibration of the UV/ion shields for the AXAF High Resolution Camera", SPIE **3114**, pp. 74-100, 1997.

Murray, S.S., and Chappell, J.H. "The AXAF High Resolution Camera", SPIE **982**, pp. 48-63, 1988.

Murray, S.S., Chappell, J.H., Kenter, A.T., Kobayashi, K., Kraft, R.P., Meehan, G.R., Zombeck, M.V., Fraser, G.W., Pearson, J.F., Lees, J.E., Brunton, A.N., Pearce, S.E., Barbera, M., Collura, A., Serio, S. "The AXAF High Resolution Camera(HRC): Calibration and Recalibration at XRCF and Beyond", SPIE **2114**, pp. 11-25, 1997.

Murray, S. *Private Communication,* 1998.

Tsiang, E. Y. *et al.* "JMKMOD: A software suite within XSPEC for the ground calibration of AXAF," in *Grazing Incidence and Multilayer X-ray Optical Systems*, R.B. Hoover and A.B. Walker, eds., *Proc SPIE* **3113**, pp. 132-141, 1997.

Tsiang, E. Y. 1997, JMKmod User Manual, publication SAO-AXAF-DR-97-276.

Wargelin, B.J., Kellogg, E.M., McDermott, W.C., Evans, I.E., Vitek, S.A. "AXAF calibration: the HXDS flow proportional counters", SPIE **3113**, pp. 526-534, 1997.

Weisskopf, M. *et al.* "Calibration of the AXAF Observatory: Overview," in *Grazing Incidence and Multilayer X-ray Optical Systems*, R.B. Hoover and A.B. Walker, eds., *Proc SPIE* **3113**, pp. 2-17, 1997.